A Hybrid Approach to Reduce Cone-Beam Artifacts for a Circular Orbit Cone-Beam CT System

SHINKOOK CHOI [1], **JINSUNG KIM**[2], **AND JONGDUK BAEK**[1], **(Member, IEEE)**
[1] School of Integrated Technology, Yonsei Institute of Convergence Technology, Yonsei University, Incheon 21983, South Korea
[2] Department of Radiation Oncology, Yonsei Cancer Center, Yonsei University College of Medicine, Seoul 03722, South Korea

Corresponding authors: Jinsung Kim (jingsung@yuhs.ac) and Jongduk Baek (jongdukbaek@yonsei.ac.kr)

ABSTRACT In a cone-beam computed tomography (CT) system, the Feldkamp, Davis, and Kress (FDK) algorithm produces cone-beam artifacts due to insufficient object sampling in the missing cone region of frequency space. While total variation minimization-based iterative reconstruction (TV-IR) may reduce cone-beam artifacts by filling in the missing cone region, it introduces image blurring or noise increase depending on the regularization parameter. In this paper, we propose a method to reduce cone-beam artifacts through an optimal combination of FDK and TV-IR images. The method utilizes FDK (TV-IR) data outside (inside) the missing cone region, which enables to keep the original image quality of the FDK image and preserve the advantages of the TV-IR image for cone-beam artifact reduction. To validate the proposed method, we used numerical phantoms composed of Defrise disks, vertical plates, and star objects and assessed the image quality of FDK, TV-IR, and the proposed method using the mean squared error, contrast to noise ratio, and structural similarity with different TV-IR regularization parameters. Experimental validation was also conducted using a spine phantom with a bench-top cone-beam CT system. The results showed that the performance of the cone-beam artifacts reduction in TV-IR depended on the value of the regularization parameter, which often produced suboptimal image quality for different imaging tasks. However, the proposed method provided good image quality regardless of the regularization parameter values.

INDEX TERMS Artifact correction, computed tomography, cone-beam artifacts, reconstruction algorithms, total variation regularization.

I. INTRODUCTION

During the past few decades, technical developments in computed tomography (CT) systems have focused on reducing the scan time, which was achieved by increasing the gantry rotation speed and the number of detector rows [1]. Although more detector rows increase the volume coverage in a single gantry rotation, the subsequent increase in cone angle results in missing data in the frequency space. According to the central slice theorem [2], cone-beam CT acquires fully sampled data for an iso-centered object but produces a missing cone region in the frequency space for an off-centered object [3], as shown in Fig. 1. As a result, the Feldkamp, Davis, and Kress (FDK) algorithm produces cone-beam artifacts which become severer as the cone angle increases [4].

Two approaches have been predominantly investigated to reduce cone-beam artifacts: modifying the data acquisition geometry and improving the reconstruction algorithm. Changing the data acquisition trajectory (such as circle and line, and saddle and helical orbits) helps to reduce the missing data samples [5]–[9], and modifying the data acquisition geometry such as inverse geometry CT (IGCT) is effective for reducing cone-beam artifacts [10]–[15]. However, these approaches require a long scan time or significant modification of the conventional CT system.
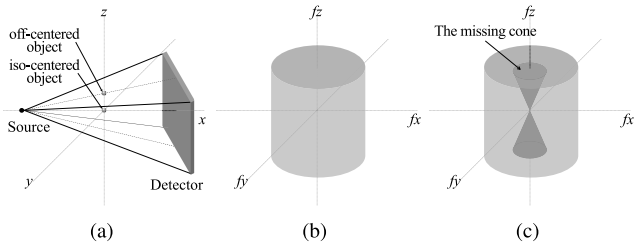
FIGURE 1. (a) The geometry of the cone-beam CT system and the sampled data (b) for an iso-centered object and (c) for an off-centered object in the frequency space.
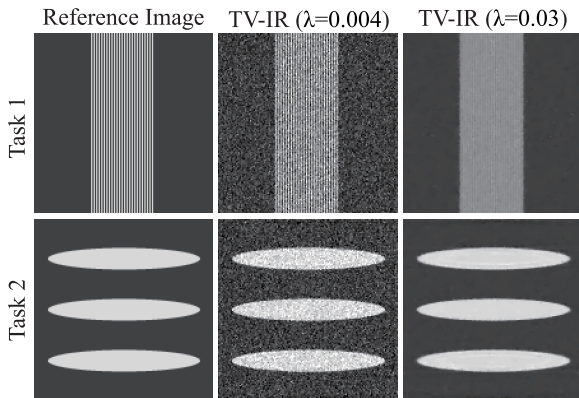

FIGURE 2. A sample coronal image of TV-IR for the two tasks. TV-IR had optimal λ values of 0.004 and 0.03 in tasks 1 and 2, respectively. The display window is [0.18 to 0.26 cm^{-1}].

In contrast, algorithmic approaches can be easily adapted to a conventional CT system, and thus several modified FDKs (e.g., parallel-FDK, tent-FDK, and weighted-FDK) have been developed [16], [17]. While they are effective in cone-beam artifacts reduction with a moderate cone angle (i.e., less than 5°), noise amplification and limited performance in cone-beam artifacts reduction with a large cone angle are issues that need to be solved [18], [19]. For a large cone angle, total variation minimization-based iterative reconstruction (TV-IR) is an effective approach for cone-beam artifacts reduction [20]–[23]. However, TV-IR may produce either over-smoothed or noise-enhanced images depending on the regularization parameter (i.e., λ). The appropriate selection of λ is important for image quality optimization in TV-IR, but an optimal λ for a specific task might not be optimal for other tasks. Fig. 2 shows the sample coronal images of TV-IR with two regularization parameters for different tasks, demonstrating that an optimal λ value is task dependent.

In this paper, we propose an algorithm to reduce the cone-beam artifacts in FDK through an optimal combination of the FDK and TV-IR images where the original image quality of the FDK and the performance of the cone-beam artifacts reduction in TV-IR are preserved in the combined image regardless of the λ in TV-IR method. The proposed method was validated using numerical phantoms including

various object structures and quantitatively evaluated using the mean squared error (MSE), contrast to noise ratio (CNR), and structural similarity (SSIM) [24]. Experimental results using a spine phantom are also presented for a qualitative evaluation.

II. METHODS

A. A BRIEF REVIEW OF TOTAL VARIATION MINIMIZATION-BASED ITERATIVE RECONSTRUCTION

The constrained optimization problem for TV-IR is as follows:

$$\min_f p(f) = \|Mf\text{-}g\|_2^2 + \lambda R(f) \tag{1}$$

where f is the cone-beam CT volume image, M is the forward projection operator, g is the projection data, λ is a regularization parameter, and R is a regularization term with total variation.

Here, R is defined as

$$cR(f_{i,j,k}) = \sum_{i,j,k} \sqrt{\begin{array}{c}(f_{i+1,j,k} - f_{i,j,k})^2 \\ + (f_{i,j+1,k} - f_{i,j,k})^2 \\ + (f_{i,j,k+1} - f_{i,j,k})^2\end{array}} \tag{2}$$

where the cone-beam CT image f is discretized on a 3-D grid with indices i, j, and k along the x, y, and z directions, respectively. Eq. (1) is solved using the Gradient Projection Barzilai-Borwen (GPBB) algorithm [25], [26]. We used the forward projector proposed by Gao [27], which was implemented with GPU hardware (NVIDIA Tesla S2050) using parallel computing to minimize the calculation time.

B. THE PROPOSED METHOD

The basic idea of the proposed method is to fill in the missing cone region of the FDK image using data reconstructed by the TV-IR method. Since the missing cone region increases as the cone angle increases, the region filled in by the TV-IR image is taken differently depending on the cone angle. As a result, the combined image retains the data for the FDK image outside the missing cone region and preserves the estimated data from the TV-IR method in the missing cone region.

The proposed method is as follows:

*Step 1:* Perform 3D FDK reconstruction f_{FDK} and TV-IR f_{TV}.

Step 2: Apply a window function to the reconstructed image to generate subvolumes:

$$f_{FDK,n} = w_n f_{FDK} \tag{3}$$

$$f_{TV,n} = w_n f_{TV} \tag{4}$$

where w_n is a window function to divide the reconstructed volumes into n subvolumes ($n = 1, 2, ..., m$). Here, m is the number of mask sets as described later. The window function is defined as

$$w_n(z) = \begin{cases} 0 & \text{if } |z| < z_{n-1}, |z| > z_n \\ 1 & \text{if } z_{n-1} \leq |z| \leq z_n \end{cases} \tag{5}$$
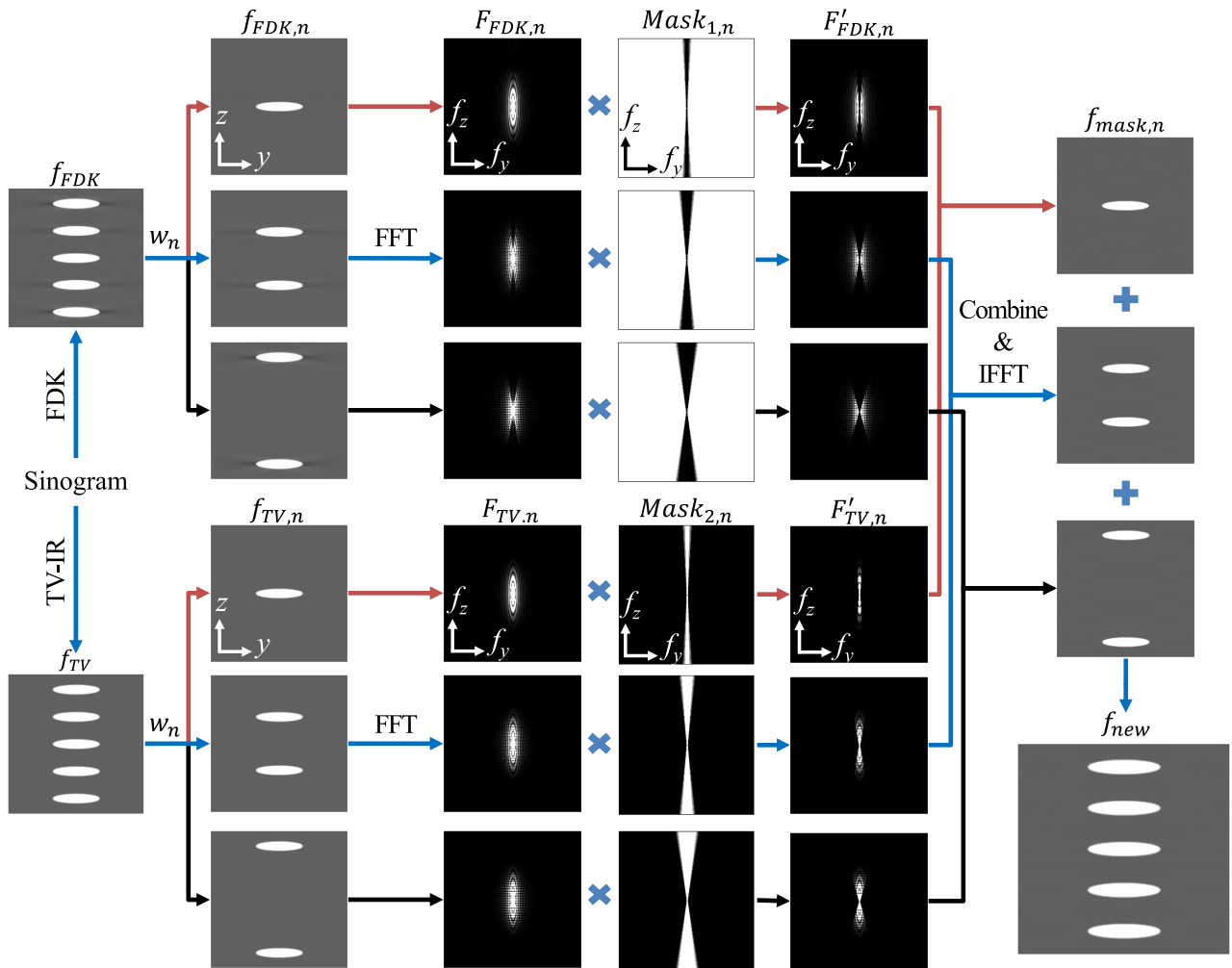
FIGURE 3. A schematic of the proposed method. In each step, the *y*-*z* plane in the image domain and the f_y-f_z plane in the frequency domain are displayed.

where $z_0 = 0$ and z_n determines the boundary of the window function along the *z* direction for the subvolumes.

Step 3: Take the 3D Fourier transform (FFT) of the FDK and TV-IR subvolumes:

$$F_{FDK,n} = FFT(f_{FDK,n}) \qquad (6)$$

$$F_{TV,n} = FFT(f_{TV,n}) \qquad (7)$$

Step 4: For the *n*th subvolume, construct a mask set based on the maximum cone angle $\theta_{max,n}$ of each subvolume in the frequency space and perform a masking process:

$$F'_{FDK,n} = Mask_{1,n}F_{FDK,n} \qquad (8)$$

$$F'_{TV,n} = Mask_{2,n}F_{TV,n} \qquad (9)$$

where $Mask_{1,n}$ ($Mask_{2,n}$) is the mask to preserve data outside (inside) the missing cone region.

Step 5: For the *n*th subvolume, add Eqs. 8 and 9 and take the 3D inverse Fourier transform (IFFT):

$$f_{mask,n} = IFFT(F'_{FDK,n} + F'_{TV,n}) \qquad (10)$$

Step 6: Add all of the subvolumes to produce the final image volume:

$$f_{new} = \sum_{n=1}^{m} f_{mask,n} \qquad (11)$$

The overall scheme for the proposed method is illustrated in Fig. 3 in which three subvolumes are selected to describe the proposed method.

C. MASK GENERATION

For optimal combination of the FDK and TV-IR images, mask sets were generated based on the maximum cone angle for each subvolume.

The maximum cone angle for the *n*th subvolume is defined as

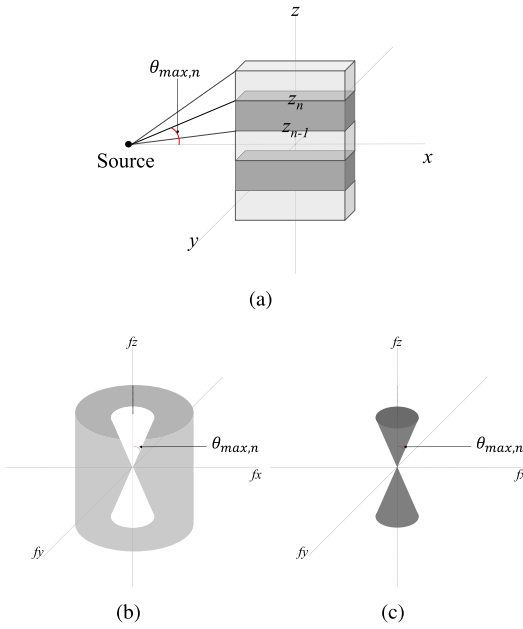$$\theta_{max,n} = \tan^{-1}\left(\frac{z_n}{SID - D}\right) \qquad (12)$$

FIGURE 4. (a) The *n*th subvolume and the corresponding mask set for (b) FDK and (c) TV-IR images.

FIGURE 5. Illustrations of the phantoms: the axial (*x-y* plane), coronal (*y-z* plane), and sagittal (*x-z* plane) images of (a) the entire phantom, (b) Phantom 1, (c) Phantom 2, and (d) Phantom 3. The display window is [0 to 0.35 cm^{-1}].

where *SID* represents the source to iso-center distance and *D* is half of the reconstructed volume size in the *x* direction.

Since the FDK algorithm produces the exact dataset outside the missing cone region, we define the mask sets as follows:

$$Mask_{1,n} = \begin{cases} 1 & \text{if } f_r > f_{r_3} \\ 2/3 & \text{if } f_{r_2} < f_r \leq f_{r_3} \\ 1/3 & \text{if } f_{r_1} < f_r \leq f_{r_2} \\ 0 & \text{if } f_r \leq f_{r_1} \end{cases} \tag{13a}$$

$$Mask_{2,n} = 1 - Mask_{1,n} \tag{13b}$$

$$f_{r_1} = f_z \tan(\theta_{max,n}) \tag{14a}$$

$$f_{r_2} = f_z \tan(\theta_{max,n} + 1°) \tag{14b}$$

$$f_{r_3} = f_z \tan(\theta_{max,n} + 2°) \tag{14c}$$

where $f_r = \sqrt{f_x^2 + f_y^2}$. The masks are designed to have a smooth transition at the boundary of the missing cone region to avoid artifacts caused by sharp transitions in the frequency space. Fig. 4 depicts a mask set for the *n*th subvolume. To determine the number of mask sets (i.e., *m*), we track the value of structural dissimilarity (DSSIM) as a function of *m* between the FDK image and the image by the proposed method, and select the *m* producing the largest DSSIM defined as

$$DSSIM(I_{fdk}, I_{combined}) = \frac{1 - SSIM(I_{fdk}, I_{combined})}{2} \tag{15}$$

where I_{fdk} is the FDK image and $I_{combined}$ is the image reconstructed by the proposed method for the coronal image of the subvolume which contains the most severe cone-beam artifacts.
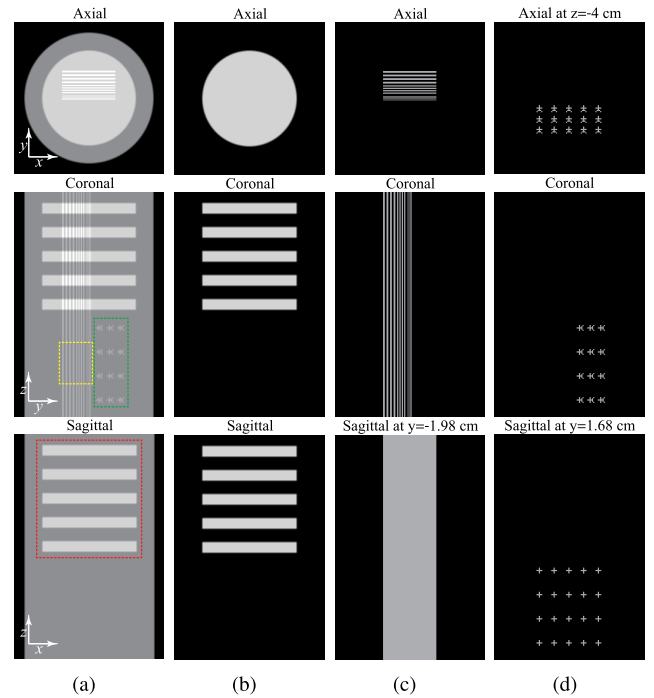
D. SIMULATIONS

To validate the proposed method, we used a phantom composed of a cylinder, Defrise disks, vertical plates, and star objects with a maximum cone angle of 13.29°, as shown in Fig. 5. The Defrise disk phantom is widely used to examine the effect of cone-beam artifacts because most of the energy is concentrated within the missing cone region in the frequency space. The vertical plate phantom has a constant value along the *z* direction, and so all energy is distributed within the f_x-f_y plane in the frequency space. The star-shaped phantom is selected since its energy is spread over all frequency regions. Fig. 6 shows the magnitude of each phantom in the frequency space.

To generate projection datasets, a numerical phantom was constructed using 1024 × 1024 × 2048 voxels and voxel binning was performed into 256 × 256 × 512 voxels to avoid discretization errors during the forward projection [28]. The geometry of each phantom is described in Table 1. The finite X-ray focal spot and detector cell size were modeled with 5 × 5 source and detector lets [29]. The projection data were calculated using Gao's method [27] and uniform Poisson noise with 2500 photons per detector cell were added. For the FDK reconstruction, the projection data were filtered with an unweighted ramp filter and voxel-driven backprojection using linear interpolation was performed. With the TV-IR method, the iteration was terminated when TV-IR yielded a steady convergence solution in terms of the mean squared error measurements. The image was reconstructed

TABLE 1. Phantom geometry characteristics.

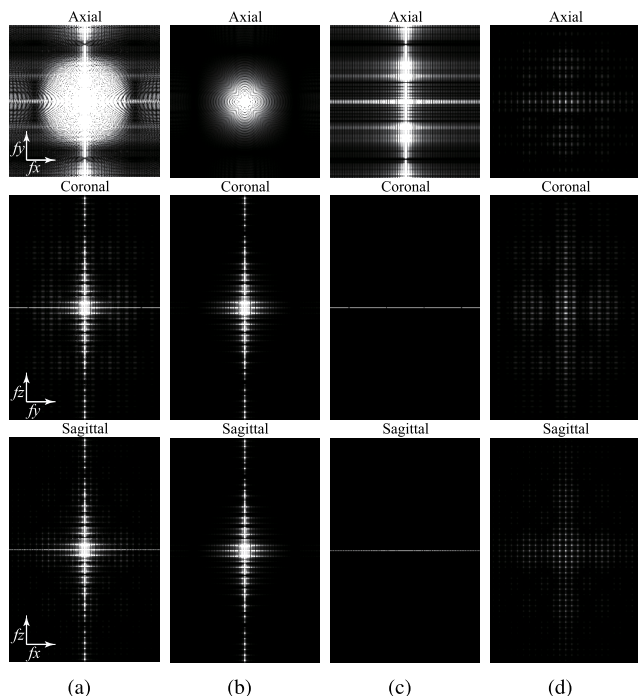| Phantom	Type	Attenuation coefficient (cm^{-1})	Radius (cm)	Thickness (mm)	Distance between centers of each object in the (x,y,z) directions (mm)
Background	Cylinder	0.2	10.9	-	-
1	Defrise	0.3	7.9	17.8	(0, 0, 40.5)
2	Vertical plates	0.25	-	2.97	(0, 5.93, 0)
			-	1.98	(0, 3.96, 0)
			-	0.99	(0, 1.98, 0)
3	Star shape	0.25	-	1.98	(24.7, 17.8, 40.5)

FIGURE 6. Magnitude of (a) the entire phantom, (b) Phantom 1, (c) Phantom 2, and (d) Phantom 3 in the frequency space. The display window is [0 to 500 cm²].

FIGURE 7. The plots of window function for the *n*th subvolume in the *z* direction.

TABLE 2. Simulation parameters used in the study.

Source to detector distance	146 cm
Detector to iso-center distance	53 cm
Detector cell size	1.552×1.552 mm^2
Detector array size	256×384
Number of views	400 views
Reconstructed volume size	$25.3 \times 25.3 \times 38$ cm^3
Reconstructed voxel size	$0.989 \times 0.989 \times 0.989$ mm^3 ($256 \times 256 \times 384$)
Regularization parameter (λ)	$0.002 : 0.002 : 0.03$

using $256 \times 256 \times 512$ voxels with the central $256 \times 256 \times 384$ voxels extracted to remove longitudinal truncation. To improve the computational speed of the TV-IR method, we used a 1.552×1.552 mm^2 detector cell size, which was relatively larger than the pixel size of the clinical cone-beam CT detector. The simulation parameters are summarized in Table 2.

To apply the proposed method, the reconstructed image was segmented into six subvolumes (i.e., maximum DSSIM with $m = 6$) using the window function in Eq. 5, where z_n was 16.8, 50.4, 84, 117.6, 151.3, and 189.8 mm with maximum cone angles of 1.20°, 3.59°, 5.97°, 8.33°, 10.66°, and 13.29°, respectively. Figs. 7 and 8 show the window function and the mask images generated for each subvolume using the maximum cone angle. The generated window function and mask sets were applied to the reconstructed FDK and TV-IR images to obtain a final image.
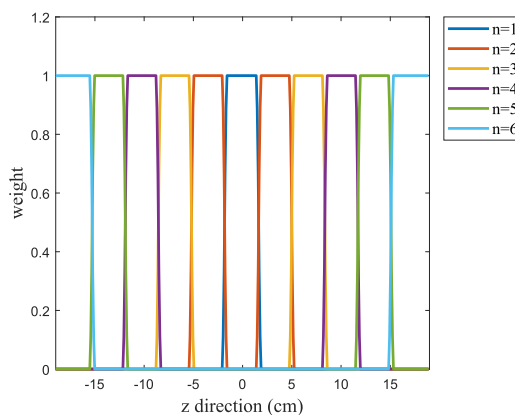
E. EXPERIMENTS

The bench-top cone-beam CT system included a generator (Indico 100, CPI Communication & Medical Products Division, Georgetown Ontario, Canada), a tungsten target X-ray source (Varian G-1592, Varian X-ray Product, Salt Lake City, UT) with a 0.6×0.6 mm^2 focal spot, and a 400×300 mm^2 flat-panel detector (PaxScan 4030CB, Varian Medical Systems, Salt Lake City, UT) with an anti-scatter grid (Philips Medical Systems, Best, the Netherlands), as shown in Fig. 9. To improve the computational speed of the TV-IR method, the projection data were acquired with 8×8 binning mode, which produced 1.552×1.552 mm^2 pixel size. The experimental parameters are summarized in Table 3. The spine phantom (PR 130, Quart, Zorneding, Germany) shown in Fig. 9 was scanned and the proposed method was applied.
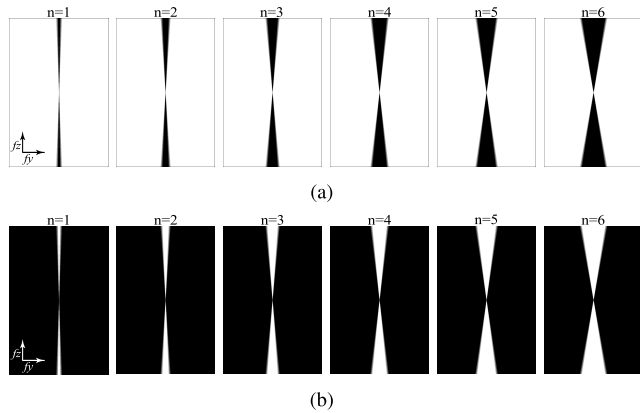
FIGURE 8. The f_y-f_z plane of (a) $Mask_{1,n}$ and (b) $Mask_{2,n}$ for each subvolume.
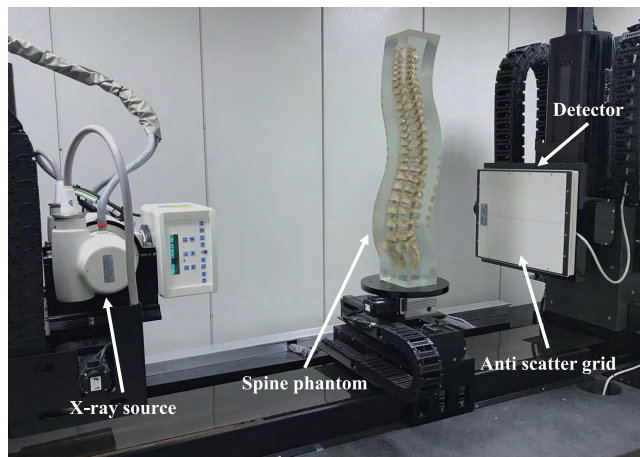

FIGURE 9. The bench-top cone-beam CT system with an anti-scatter grid and a spine phantom.

TABLE 3. Experimental parameters used in the study.

Source to detector distance	120 cm
Detector to iso-center distance	40 cm
Focal spot size of X-ray source	0.6×0.6 mm^2
X-ray source operating mode	90 kVp, 2mA
Detector operating mode	8×8 binning
Detector cell size	1.552×1.552 mm^2
Detector array size	256×192
Detector frame rate	10 fps
Number of views	400 views
Reconstructed volume size	$26.5 \times 26.5 \times 19.9$ cm^3
Reconstructed voxel size	$1.035 \times 1.035 \times 1.035$ mm^3 ($256 \times 256 \times 192$)
Regularization parameter (λ)	0.0001, 0.004, 0.06

Due to the presence of the anti-scatter grid, the detector center was aligned to the X-ray source, and thus the maximum cone angle (8.46°) was relatively smaller than our simulation setting. For the experimental data, the number of mask sets was selected as four (i.e., $m = 4$) since DSSIM was maximized with $m = 4$.
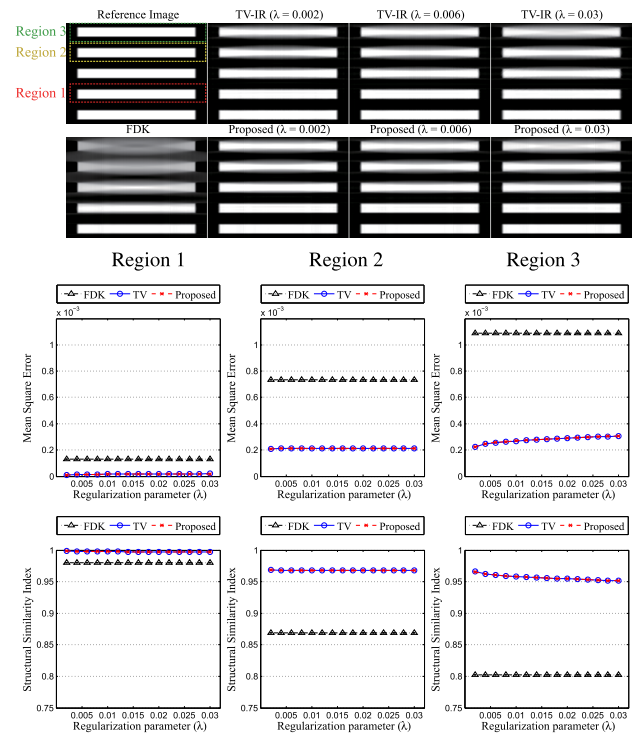

FIGURE 10. Sample images and MSE and SSIM values reconstructed by FDK, TV-IR, and the proposed method from the results of Phantom 1. The display window of the sample images is [0.2 to 0.3 cm^{-1}].

F. IMAGE QUALITY ASSESSMENT

To analyze the image quality of FDK, TV-IR, and the proposed method, we selected a region of interest for each phantom, as shown in Fig. 5(a) (indicated by the red, yellow, and green boxes). The quality of the final image was influenced by the estimation performance of the TV-IR within the missing cone region, which was controlled by λ. Note that using a larger λ value reduced the image noise but increased image blurring.

Thus, the effect of the TV-IR method on cone-beam artifacts reduction and image blurring was analyzed using reconstructed images of noiseless projection data. The noise effect was analyzed further using reconstructed images of noisy projection data. For each phantom, the image quality was assessed using MSE, CNR, and SSIM. The image quality was calculated from 30 independent noise realizations and the averaged values were reported.
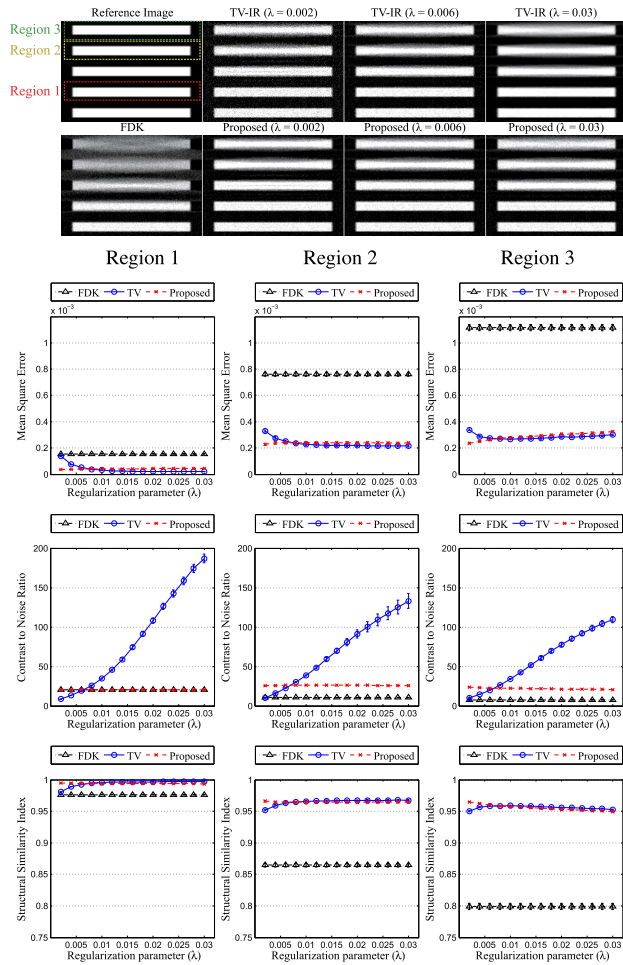
MSE is defined as

$$\text{MSE} = \frac{1}{L} \sum_{l=1}^{L} (f(l) - f_{ref}(l))^2 \qquad (16)$$

where f is the intensity value of the reconstructed volume at pixel l, f_{ref} is the intensity value of the reference volume at pixel l, and L denotes the number of image pixels.

CNR is defined as

$$\text{CNR} = \frac{|\mu_{obj} - \mu_{bg}|}{\sigma_{noise}} \qquad (17)$$

FIGURE 11. Sample images reconstructed by FDK, TV-IR, and the proposed method from the noisy projection data of Phantom 1. The display window of the sample images is [0.2 to 0.3 cm^{-1}]. The MSE, CNR, and SSIM results are reported with 95% confidence intervals.

FIGURE 12. Sample images, and MSE and SSIM values reconstructed by FDK, TV-IR, and the proposed method from the noiseless results of Phantom 2. The display window of the sample images is [0.2 to 0.27 cm^{-1}].

where μ_{obj} and μ_{bg} are the mean intensity of the object and the background regions of each phantom, respectively, and σ_{noise} is the standard deviation of the noise in the background region.
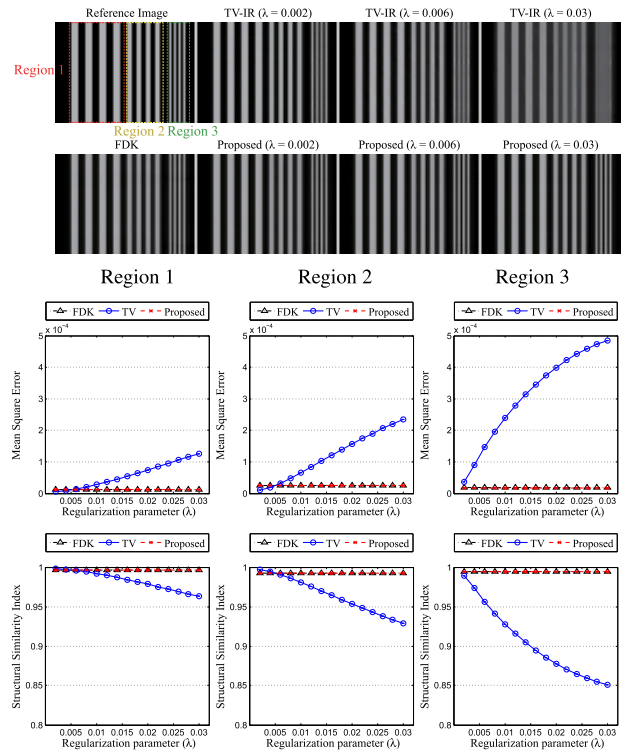
SSIM is defined as

$$\text{SSIM}(a, b) = \frac{(2\mu_a\mu_b + c_1)(2\sigma_{ab} + c_2)}{(\mu_a^2 + \mu_b^2 + c_1)(\sigma_a^2 + \sigma_b^2 + c_2)} \quad (18)$$

where μ_a and σ_a are the mean intensity and standard deviation of reconstructed image a, respectively; μ_b and σ_b are the mean intensity and standard deviation of reference image b; σ_{ab} is the covariance between reconstructed image a and reference image b; and c_1 and c_2 are constant values. In our calculation, we used $c_1 = 6.5 \times 10^{-4}$ and $c_2 = 2.6 \times 10^{-3}$.

III. RESULTS
For the visual inspection of the image quality improvement by TV-IR and the proposed method in the numerical phantom study, we show the sample images with three λ values (i.e., 0.002, 0.006, and 0.03). Note that the image noise variance of

the TV-IR was similar to that of FDK in the axial plane with a λ value of 0.006. We performed a quantitative evaluation using three regions for each numerical phantom. Regions 1, 2, and 3 of Phantoms 1 and 3 had maximum cone angles of 4.29°, 9.98°, and 13.29°, respectively.

Fig. 10 depicts a comparison of the reconstructed noiseless image of Phantom 1 using FDK, TV-IR with three λ values, and the proposed method. The MSE and SSIM for each region are plotted for different λ values. It is evident that the TV-IR method introduces more blurring as the λ value increased. It can also be seen that the cone-beam artifacts are reduced by the TV-IR method. The MSE of FDK is the highest among the methods and increases as the cone angle increased. In contrast, TV-IR shows reduced MSE due to its ability to fill in the missing cone region. It is also apparent that using a larger λ value increases the MSE of TV-IR due to the increased image blurring effect despite its contribution to cone-beam artifacts reduction. This phenomenon is clearly visible in the MSE plot of Region 3. The MSE of the proposed method follows that of the TV-IR method in all regions and its SSIM shows a similar trend to its MSE.
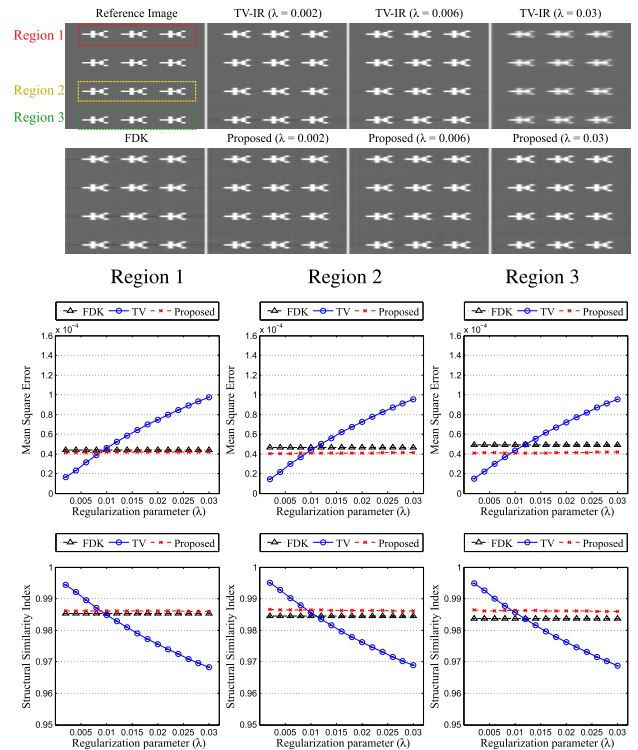
When the image is reconstructed using noisy projection data, TV-IR with a small λ value produces higher image noise than that of the FDK image, as shown in Fig. 11. As a result, the MSE of the proposed method is lower than that of the TV-IR method with λ values of less than 0.006 because the
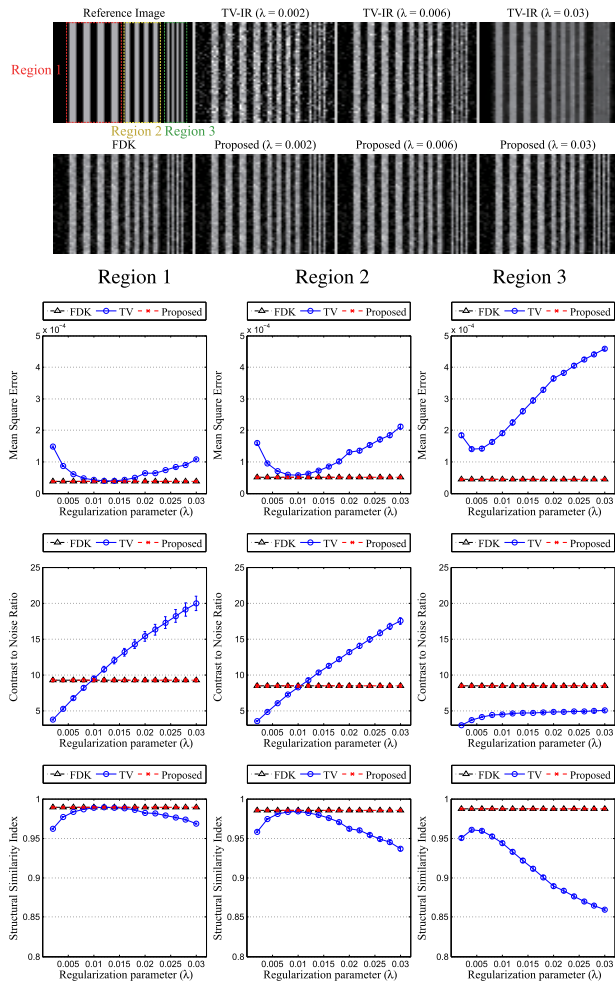
FIGURE 13. Sample images reconstructed by FDK, TV-IR, and the proposed method from the noisy projection data of Phantom 2. The display window of the sample images is [0.2 to 0.27 cm^{-1}]. The MSE, CNR, and SSIM results are reported with 95% confidence intervals.
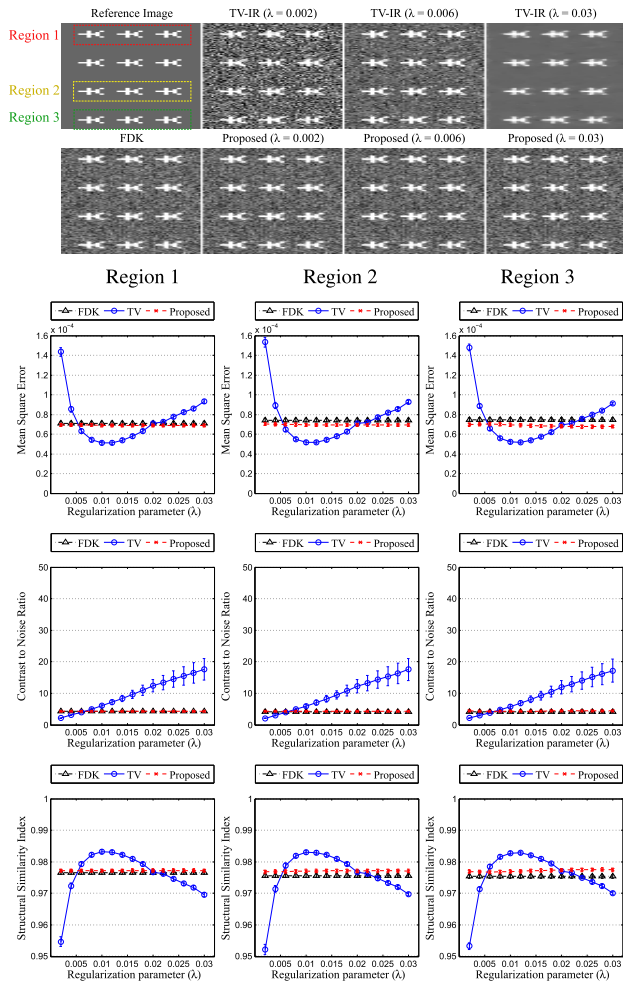

FIGURE 14. Sample images, and MSE and SSIM values reconstructed by FDK, TV-IR, and the proposed method from the noiseless results of Phantom 3. The display window of the sample images is [0.18 to 0.23 cm^{-1}].

increased noise of TV-IR is only reflected in the missing cone region for the proposed method. As the λ value increases, the image noise is reduced, and thus TV-IR and the proposed method show similar MSE values. While the SSIM of TV-IR displays a similar trend to its MSE, its CNR increases as the λ value increases and becomes higher than that of the proposed method when the λ value is larger than 0.006. This result mainly stems from the reduced noise effect of TV-IR with larger λ values.

Fig. 12 shows a comparison of the reconstructed noiseless image of Phantom 2 using FDK, TV-IR with three λ values, and the proposed method. The MSE and SSIM for each region are plotted as well. FDK produces an exact reconstructed image since the energy of Phantom 2 is distributed within the $f_x f_y$ plane. In contrast, TV-IR results in image blurring, which becomes severer as the λ value increases. As a result, the MSE of TV-IR is higher than that of FDK for Regions 1 and 2 when λ is greater than 0.006 and for Region 3 at all λ values. It is evident that the proposed method follows the performance of

FDK due to the selective usage of data from FDK and TV-IR. Furthermore, the SSIM shows a similar trend to the MSE.

When noise is added, the MSE of TV-IR remains higher than that of FDK and the proposed method in all regions, as shown in Fig. 13. While the MSE of TV-IR with noiseless data increases as the λ value increases, the MSE of TV-IR with noisy data follows a parabolic shape as the λ value increases, because the effects of noise reduction and image blurring on image quality compete with each other. Like Phantom 1, the CNR of TV-IR increases as the λ value increases. Note that using a large λ value is not the right choice for the vertical plate phantom in Region 3 due to the significant image blurring of TV-IR. Overall, the SSIM shows a similar trend to the MSE for noisy data.

The reconstructed noiseless images of Phantom 3 along with MSE and SSIM plots are shown in Fig. 14. Since the proposed method reduces the cone-beam artifact while retaining the sharpness of the objects, the performance of the proposed method is suboptimal when λ is less than 0.008. However, the image blurring of TV-IR with a λ value larger than 0.008 introduces more errors in the missing cone regions, and thus the MSE and SSIM of the proposed method are better than those of TV-IR. However, when noise is added, the optimal λ values of the proposed method are changed, as shown in Fig. 15, and the MSE and SSIM of the proposed method are better with λ values of less than 0.006 or larger
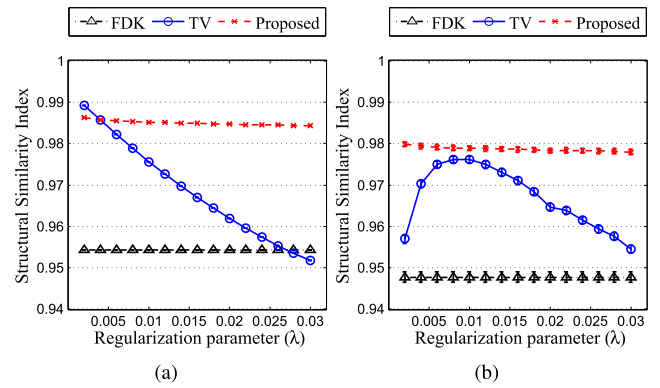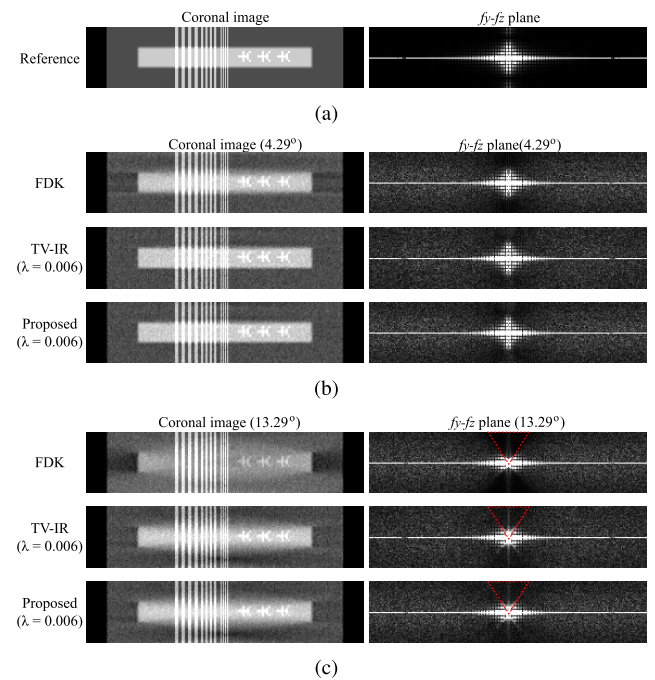
FIGURE 15. Sample images reconstructed by FDK, TV-IR, and the proposed method from the noisy projection data of Phantom 3. The display window of the sample images is [0.18 to 0.23 cm^{-1}]. The MSE, CNR, and SSIM results are reported with 95% confidence interval.


FIGURE 16. Averaged SSIM values of (a) noiseless and (b) noisy results.

FIGURE 17. (a) A reference coronal image and the corresponding f_y-f_z plane. The coronal image examples contained three phantoms and the corresponding f_y-f_z plane of the subvolume with a maximum cone angle of (b) 4.29° and (c) 13.29° from FDK, TV-IR, and the proposed method. The display windows of the coronal images and frequency responses are [0.15 to 0.35 cm^{-1}] and [0 to 150 cm^2], respectively. The red dotted line indicates the missing cone region.

than 0.02. Since the signal energy of the star-shaped phantom is spread over all frequency regions, the positive (i.e., noise reduction and filling in the missing cone region) and negative (i.e., image blurring) effects of TV-IR contribute differently to the final image quality for different λ values. Note that the CNR of TV-IR increases as the λ value increases due to reduced image noise.

The results in Figs. 10-15 indicate that the optimal λ value depends on the imaging task, which would have been more significant when the object contains various structures. To assess the overall image quality of the entire phantom, we calculated the averaged SSIM of Phantoms 1, 2, and 3 since SSIM provided a normalized image quality metric for different tasks. As shown in Fig. 16, the proposed method provides the highest averaged SSIM values for all λ values except for 0.002 with noiseless data, and it has the highest averaged SSIM values for all λ values with noisy data. Fig. 17 shows examples of the coronal images of the subvolumes containing all three phantoms reconstructed by FDK, TV-IR,

and the proposed method for cone angles of 4.29° and 13.29°, and the corresponding f_y-f_z plane of the subvolumes. It can be seen that FDK produces the missing cone region with the subvolume of 13.29° cone angle, but TV-IR fills in the missing cone region. The proposed method selectively takes the data of FDK and TV-IR, thereby achieving the highest averaged SSIM value.

To examine the image quality of the combined image of the experimental spine phantom, FDK was performed using two different interpolation methods during the backprojection: linear (i.e., FDK (linear)) and four-fold Fourier interpolation (i.e., FDK (Fourier)) [29]. Note that FDK (Fourier) produces
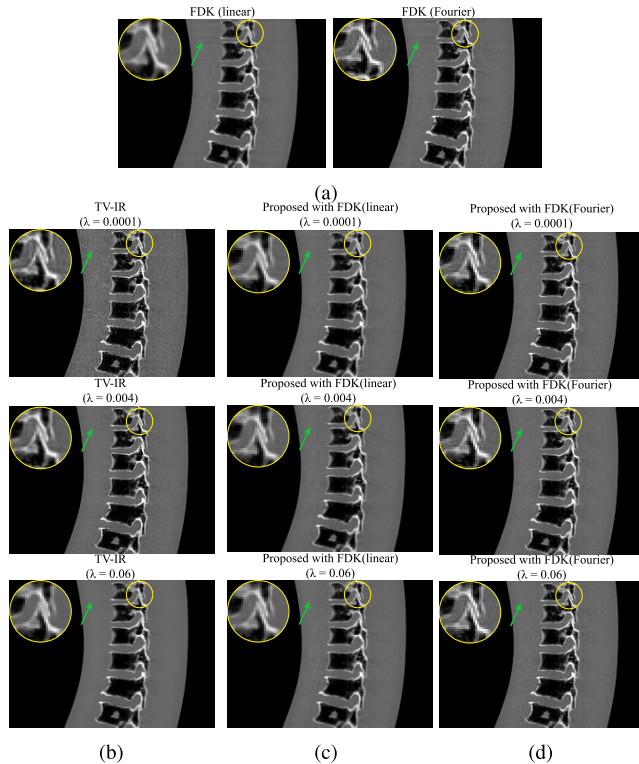
FIGURE 18. Coronal images reconstructed by (a) FDK using linear interpolation and four-fold Fourier interpolation, (b) TV-IR, and the proposed method with FDK using (c) linear interpolation and (d) four-fold Fourier interpolation. The upper left corner of each image shows a magnified view of the yellow circled region. The green arrow indicates the region of the cone-beam artifacts present in the FDK image. The display window is [0.1 to 0.4 cm^{-1}].

a much sharper image than FDK (linear) due to the sinc interpolation during the backprojection. Fig. 18 shows the reconstructed coronal images of the spine phantom using FDK (linear), FDK (Fourier), TV-IR with three λ values (0.0001, 0.004, and 0.06), and the proposed method. Note that the image noise variance of TV-IR with a λ value of 0.004 was similar to that of FDK (linear) in the axial plane. FDK (linear) and FDK (Fourier) produce cone-beam artifacts whereas TV-IR and the proposed method reduce them effectively, as shown by the green arrow in Fig. 18. While the coronal images of TV-IR show higher noise with a λ value of 0.0001 and image blurring with a λ value of 0.06, the proposed method preserves the original image quality of the FDK images for all λ values, as shown by the yellow circle in Fig. 18. Overall, the proposed method provides equivalent image quality to the FDK image with reduced cone-beam artifacts.

IV. DISCUSSION AND CONCLUSIONS

A new method to reduce cone-beam artifacts by the optimal combination of FDK and TV-IR images was proposed. The proposed method utilizes FDK and TV-IR images selectively in the frequency space, which enables to retain the original image quality of FDK and preserve the advantages of TV-IR

in cone-beam artifact reduction. As demonstrated by our results, it is important to optimize the regularization parameters of TV-IR because its image quality is determined by the balance between the image blurring effect and noise suppression. However, it is not feasible to optimize the image quality of TV-IR using a single regularization parameter for objects with complex structures. On the other hand, the proposed method is less influenced by the regularization parameter than TV-IR and shows overall good image quality.

The proposed method constructs mask sets for filtering FDK and TV-IR images. We used six (four) mask sets when attaining the simulation (experimental) data, but the choice of the number of masks is task dependent. In this work, the mask sets were defined using a step function in the frequency transition region. Another alternative is to use a smooth function (e.g., the cosine function) to obtain a smoother transition in the frequency region. Since the number of pixels within the frequency transition region was small (i.e., less than 5), the performance of the proposed method is similar regardless of the mask transition type. If the frequency transition region becomes larger, using a smooth function would be desirable to avoid residual artifacts caused by the data combination in the frequency space.

In our results, the image quality of the combined image used in the proposed method followed that of FDK because the maximum cone angle was about 13°, which was only 7% of the entire dataset. However, if the cone angle is very large (e.g., in an industrial CT system with a cone angle of more than 30°), a more sophisticated technique in data combination would be necessary to provide similar texture and noise property to that of the FDK image. One possible solution is to conduct modulation transfer function (MTF) matching between the FDK and TV-IR images using the MTF of the FDK at the iso-center. For a specific cone angle, the MTF of the TV-IR can be calculated, and the MTF ratio can be calculated by dividing the MTF of the FDK at the iso-center by that of TV-IR. Subsequently, this ratio is applied to the combined volume in the missing cone region, which might be helpful for providing similar texture and noise property of the combined image to those of the FDK image.

In TV-IR, the data fidelity term is more important than the regularization term in reducing cone-beam artifacts, and unregularized IR may provide the best performance in cone-beam artifacts reduction [20]. However, noise is inevitable in real data measurement, and thus the regularization term is beneficial for achieving optimal image quality. In this work, we used the TV-IR method with a regularization parameter range from 0.002~0.03. Although not presented in this paper, we evaluated the image quality of the combined image by the proposed method using a much larger parameter space (i.e., 0.002~0.3). The results showed that the performance of TV-IR varied significantly for different regularization parameter values, but the proposed method still provided stable performance for the extended parameter space. Using images reconstructed with more advanced algorithms such as model-based iterative reconstruction and

deep-learning based reconstruction [31], [32] could be used to improve the performance of the proposed method.

In our simulation, the forward projector was designed without considering the characteristics of the X-ray source. Polychromatic X-ray spectra and scattered X-ray photons degraded the image quality due to beam-hardening and scatter artifacts. In our experiment, we used an anti-scatter grid to reduce the scattered photons. However, a small number of scattered photons were present in the real data measurements, which seemed to hinder the visualization of the cone-beam artifacts. This effect would be more significant for scanning much larger phantoms, and thus appropriate scatter correction techniques (e.g., beam-absorber array method [33], primary modulation method [34], and scatter kernel models [35], [36]) would be necessary before applying the proposed method.

In conclusion, we proposed a new method that combines FDK and TV-IR images to retain the data of the FDK images and to reduce cone-beam artifacts. We observed that the proposed method obtained good image quality overall with various object structures regardless of the regularization parameters.

REFERENCES

[1] K. Taguchi and H. Aradate, "Algorithm for image reconstruction in multi-slice helical CT," *Med. Phys.*, vol. 25, no. 4, pp. 550–561, 1998.

[2] A. C. Kak and M. Slaney, *Principles Computerized Tomographic Imaging*. Philadelphia, PA, USA: SIAM, 2001.

[3] J. Hsieh, "A practical cone beam artifact correction algorithm," in *Proc. IEEE Nucl. Sci. Symp. Conf. Rec.*, vol. 2, Oct. 2000, pp. 15–71.

[4] L. A. Feldkamp, L. C. Davis, and J. W. Kress, "Practical cone-beam algorithm," *J. Opt. Soc. Amer. A, Opt. Image Sci.*, vol. 1, no. 6, pp. 612–619, 1984.

[5] G. L. Zeng and G. Gullberg, "A cone-beam tomography algorithm for orthogonal circle-and-line orbit," *Phys. Med. Biol.*, vol. 37, no. 3, p. 563, 1992.

[6] C. Bontus, T. Köhler, and R. Proksa, "A quasiexact reconstruction algorithm for helical CT using a 3-Pi acquisition," *Med. Phys.*, vol. 30, no. 9, pp. 2493–2502, 2003.

[7] A. Katsevich, "An improved exact filtered backprojection algorithm for spiral computed tomography," *Adv. Appl. Math.*, vol. 32, no. 4, pp. 681–697, May 2004.

[8] J. D. Pack, F. Noo, and H. Kudo, "Investigation of saddle trajectories for cardiac CT imaging in cone-beam geometry," *Phys. Med. Biol.*, vol. 49, no. 11, p. 2317, 2004.

[9] H. Yang, M. Li, K. Koizumi, and H. Kudo, "Exact cone beam reconstruction for a saddle trajectory," *Phys. Med. Biol.*, vol. 51, no. 5, p. 1157, 2006.

[10] T. G. Schmidt, R. Fahrig, N. J. Pelc, and E. G. Solomon, "An inverse-geometry volumetric CT system with a large-area scanned source: A feasibility study," *Med. Phys.*, vol. 31, no. 9, pp. 2623–2627, 2004.

[11] J. Baek and N. J. Pelc, "Direct two-dimensional reconstruction algorithm for an inverse-geometry CT system," *Med. Phys.*, vol. 36, no. 6, pp. 394–401, 2009.

[12] J. Baek and N. J. Pelc, "A new method to combine 3D reconstruction volumes for multiple parallel circular cone beam orbits," *Med. Phys.*, vol. 37, no. 10, pp. 5351–5360, 2010.

[13] J. Baek *et al.*, "A multi-source inverse-geometry CT system: Initial results with an 8 spot X-ray source array," *Med. Phys.*, vol. 59, no. 5, p. 1189, 2014.

[14] J. Baek, B. De Man, D. Harrison, and N. J. Pelc, "Raw data normalization for a multi source inverse geometry CT system," *Opt. Express*, vol. 23, pp. 7514–7526, Mar. 2015.

[15] B. De Man *et al.*, "Multisource inverse-geometry CT. Part I. System concept and development," *Med. Phys.*, vol. 43, no. 8, pp. 4607–4616, 2016.

[16] M. Grass, T. Köhler, and R. Proksa, "3D cone-beam CT reconstruction for circular trajectories," *Phys. Med. Biol.*, vol. 45, no. 2, p. 329, 2000.

[17] Z. Chen, V. D. Calhoun, and S. Chang, "Compensating the intensity fall-off effect in cone-beam tomography by an empirical weight formula," *Appl. Opt.*, vol. 47, no. 37, pp. 6033–6039, 2008.

[18] S. Valton, F. Peyrin, and D. Sappey-Marinier, "Analysis of cone-beam artifacts in off-centered circular ct for four reconstruction methods," *Int. J. Biomed. Imag.*, vol. 2006, p. 80421, Aug. 2006.

[19] L. Li, Y. Xing, Z. Chen, L. Zhang, and K. Kang, "A curve-filtered FDK (C-FDK) reconstruction algorithm for circular cone-beam CT," *J. X-Ray Sci. Technol.*, vol. 19, no. 3, pp. 355–371, 2011.

[20] C. Maaß, F. Dennerlein, F. Noo, and M. Kachelrieß, "Comparing short scan ct reconstruction algorithms regarding cone-beam artifact performance," in *Proc. IEEE Nucl. Sci. Symp. Conf. Rec. (NSS/MIC)*, Oct. 2010, pp. 2188–2193.

[21] D. Shi, "Successful suppression of cone beam artifacts using iterative reconstruction algorithm," in *Proc. IEEE Nucl. Sci. Symp. Med. Imag. Conf. (NSS/MIC)*, Nov. 2014, pp. 1–3.

[22] J. C. Park *et al.*, "Fast compressed sensing-based CBCT reconstruction using Barzilai-Borwein formulation for application to on-line IGRT," *Med. Phys.*, vol. 39, no. 3, pp. 1207–1217, 2012.

[23] E. Y. Sidky and X. Pan, "Image reconstruction in circular cone-beam computed tomography by constrained, total-variation minimization," *Phys. Med. Biol.*, vol. 53, no. 17, p. 4777, Sep. 2008.

[24] Z. Wang, A. C. Bovik, H. R. Sheikh, and E. P. Simoncelli, "Image quality assessment: From error visibility to structural similarity," *IEEE Trans. Image Process.*, vol. 13, no. 4, pp. 600–612, Apr. 2004.

[25] J. Barzilai and J. M. Borwein, "Two-point step size gradient methods," *IMA J. Numer. Anal.*, vol. 8, no. 1, pp. 141–148, 1988.

[26] M. A. T. Figueiredo, R. D. Nowak, and S. J. Wright, "Gradient projection for sparse reconstruction: Application to compressed sensing and other inverse problems," *IEEE J. Sel. Topics Signal Process.*, vol. 1, no. 4, pp. 586–597, Dec. 2007.

[27] H. Gao, "Fast parallel algorithms for the X-ray transform and its adjoint," *Med. Phys.*, vol. 39, no. 11, pp. 7110–7120, Nov. 2012.

[28] A. Goertzen, F. Beekman, and S. Cherry, "Effect of voxel size in CT simulations," in *Proc. IEEE Nucl. Sci. Symp. Conf. Rec.*, vol. 3, Oct. 2000, pp. 20–93.

[29] J. Hsieh, *Computed Tomography: Principles, Design, Artifacts, and Recent Advances*, vol. 114. Bellingham, WA, USA: SPIE, 2003.

[30] Z. Zhao, G. Gang, and J. Siewerdsen, "Noise, sampling, and the number of projections in cone-beam CT with a flat-panel detector," *Med. Phys.*, vol. 41, no. 6, p. 061909, 2014.

[31] R. C. Nelson, S. Feuerlein, and D. T. Boll, "New iterative reconstruction techniques for cardiovascular computed tomography: How do they work, and what are the advantages and disadvantages?" *J. Cardiovascular Comput. Tomogr.*, vol. 5, no. 5, pp. 286–292, 2011.

[32] H. Chen *et al.*, "Low-dose CT via convolutional neural network," *Biomed. Opt. Express*, vol. 8, no. 2, pp. 679–694, 2017.

[33] R. Ning, X. Tang, and D. Conover, "X-ray scatter correction algorithm for cone beam CT imaging," *Med. Phys.*, vol. 31, no. 5, pp. 1195–1202, 2004.

[34] L. Zhu, N. R. Bennett, and R. Fahrig, "Scatter correction method for X-ray CT using primary modulation: Theory and preliminary results," *IEEE Trans. Med. Imag.*, vol. 25, no. 12, pp. 1573–1587, Dec. 2006.

[35] P. Msaki, B. Axelsson, C. M. Dahl, and S. A. Larsson, "In spectusing point scatter distribution functions," *J. Nucl. Med.*, vol. 28, pp. 1861–1869, Dec. 1987.

[36] M. Sun and J. M. Star-Lack, "Improved scatter correction using adaptive scatter kernel superposition," *Phys. Med. Biol.*, vol. 55, no. 22, p. 6695, 2010.

SHINKOOK CHOI received the B.S. and M.S. degrees in electrical and electronic engineering from Yonsei University, Seoul, South Korea, in 2012 and 2014, respectively, where he is currently pursuing the Ph.D. degree with the School of Integrated Technology. His main fields of interests include computed tomography artifact correction and iterative reconstruction.

JINSUNG KIM received the Ph.D. degree from the Department of Nuclear and Quantum Engineering, KAIST. He started his career in the field of radiation oncology in 2007. He has gained clinical experience with proton therapy, the next generation of cancer treatment, for 10 years in the field. In 2009, he joined the Department of Radiation Oncology, Samsung Medical Center, as a Clinical Professor, where he contributed the advanced image guided proton scanning therapy. In 2016, he joined the Department of Radiation Oncology, Yonsei University, as an Assistant Professor and the Chief Physicist. He is carrying out various outstanding studies with researchers from the field of medical physics, which requires imperative fusion of medicine and engineering. He currently focuses on the research which involves the overlapping of medical imaging and radiation therapy. In addition, with 10 years of experience in proton therapy, he is in the front line of commissioning the very first heavy-ion treatment system in South Korea. He took a leading role in establishing the international cooperation with relative associations and his current working body. With these advantages, he was nominated as a member of the Young Korean Academy of Science and Technology. We expect to be able to witness a devastating increase not only in various forms of exchange with our members worldwide but also in research results between multidisciplinary courses.

Dr. Kim is a member of the Korean Society of Radiation Oncology, American Association of Physicists in Medicine, and Korean Physical Society. Being acknowledged in the academia, he serves for the academy as a Board Member and was appointed as the Secretary General for the Korean Society of Medical Physics in 2011.

JONGDUK BAEK received the B.S. degree in electrical engineering from Yonsei University, Seoul, South Korea, in 2004, and the M.S. and Ph.D. degrees in electrical engineering from Stanford University, CA, USA, in 2007 and 2009, respectively, with a focus on the development of inverse geometry computed tomography (CT). He is currently a Vice Director of the Yonsei Institute of Convergence Technology, Yonsei University, where he is also an Associate Professor with the School of Integrated Technology. His research interests include image quality assessment using mathematical observer models, CT imaging systems, medical imaging processing, and low-dose CT with a deep-learning approach.

• • •